Mobile Sensor for Clouds Shadow Detection and Direct Normal Irradiance Estimation

José M. Aguilar-López*, Ramón A. García, Adolfo J. Sánchez, Antonio J. Gallego, Eduardo F. Camacho

Departamento de Ingeniería de Sistemas y Automática, Universidad de Sevilla, Camino de los Descubrimientos s/n, 41092 Sevilla, Spain

Abstract

This paper presents a mobile sensor system to detect and estimate low direct normal irradiance (DNI) areas caused by clouds shadows. This work proposes using a team of unmanned aerial vehicles (UAVs) to localise and characterise the shadow of mobile clouds. This information can be used by the plant control system to minimise its effects over a solar plant.
Simulations to test and discuss the algorithm are presented. The work presented here obtains a similar degree of precision as far as the estimation of the shape of the cloud shadow is concerned but with a much faster computational time than other algorithms described in literature.

Keywords:
Spatial solar radiation estimation, Mobile Sensor, DNI, Multi-robot, UAV.

1. Introduction

The reduction of greenhouse gas emissions to the atmosphere is a priority for the future of the planet. In particular, solar energy is the most abundant energy source (Kannan and Vakeesan, 2016; Blanco and Santigosa, 2017). Increasing the competitiveness and efficiency of solar energy plants is one of the main challenges described by the National Academy of Engineering (Academy, 2008) for the 21st century. This problem is also pointed out by the European Commission (European Commission, 2014, 2015).

*Corresponding author: jaguilarl@us.es

Nomenclature

Acronyms

UAV Unmanned aerial vehicle.

ACO Ant colony optimisation.

DNI Direct normal irradiance.

CSP Concentrated solar power plant.

PV Photovoltaic.

GPC Generalised predictive controllers.

Hybrid Algorithm

A Surveillance area.

N, M Area grid rows and columns.

r, c Cell grid rows and columns.

τ_{ij} Repellent on cell ij.

d_{ij} Distance between cells i, j.

p_{ij}^{τ} Probability based on repellent.

p_{ij}^{d} Probability based on the distance.

I, $I(x)$, I_{th} Irradiance map, irradiance at x and irradiance threshold.

Clouds Shadow Model

C Clouds shadow.

(x_0, y_0) C center coordinates.

a, b Semi-major and semi-minor axes of the ellipse.

θ Rotation angle of the ellipse.

ε_e Eccentricity of the ellipse.

Shadow Estimation Algorithm

H, K Polytope definition matrices.

n, m Polytope number of restrictions and dimension.

Q, Q_c Polytope and polytope envelope of C.

ε Ellipsoid.

O_ε Center of the ellipsoid.

E Positive definite symmetric matrix $m \times m$.

ν m-dimensional unit ball volume.

Vol_ε Volume of the ellipsoid.

$\|\cdot\|$ Euclidean norm.

x, x_t 2D point and 2D point at time t.

V Vertices of the polytope.

N_V Number of vertices of the polytope.

δ Sigmoid function variable.

a_σ, b_σ, c_σ Sigmoid function parameters.

s Discrete derivative step.

$\overrightarrow{V_C}$ Cloud velocity vector.

The need to reduce the environmental impact of fossil energies has increased the interest in renewable energy sources during the past years. In particular, solar energy has experienced a great impulse since the beginning of the century. The increase of the size of commercial solar energy plants and the need to make the operation as efficient as possible give rise that obtaining an adequate estimation of the direct solar radiation distribution becomes a crucial issue.

The use of renewable energy sources to produce electricity has received considerable attention for the last 20 years. Many solar power plants have been built and commissioned around the world (Camacho et al., 2019). For instance, the three 50 MW Solaben and the two 50 MW Solacor parabolic trough plants of Atlantica Yield in Spain, or the SOLANA and Mojave Solar parabolic trough plants located in Arizona and California, each of 280 MW power production (Islam et al., 2018; Solar Millennium, 2018).

One of the main drawbacks when operating solar thermal plants is that the primary energy source, solar irradiance, cannot be manipulated. It depends on several factors. Some of them are predictable using mathematical models, such as the hour or location (Besharat et al., 2013). However, some of them such as meteorological factors, are intermittent. The effect of passing clouds is very difficult to be anticipated because many variables have to be known a priori: the position of the clouds (including height), wind speed and its direction, or their genera (such as cirrus, stratus, or cumulonimbus) as showed in (Matuszko, 2012).

One of the control objectives of thermosolar energy plants is to maintain the average temperature of the solar field around a set-point despite the strong disturbances (Camacho et al., 2012; Andrade et al., 2013). The effect of abrupt variation of the direct normal irradiance (DNI) affects that objective. The size of the current commercial solar plants (covering up to 780 hectares) requires predicting the future evolution of the clouds passing over the field to take adequate anticipative actions. The research done in (Camacho and Gallego, 2013; Sánchez et al., 2018b) shows that significant production and revenues can be obtained by changing the operating temperature taking into account the DNI levels. Furthermore, in (Camacho et al., 2019) a case study considering a large-scale solar trough plant shows the importance of knowing the spatial distribution of DNI. Estimating the spatial distribution of the DNI is one of the main objectives posed in the Advanced Grant OCONTSOLAR (European Commission, 2018) funded by the European Research Council.

There are many methods to measure or forecast spatial DNI. In (Dersch et al., 2019), ground-based measurements, forecast datasets provided from the European Centre for Medium-Range Weather Forecast, and a new method combining differents nowcasting methods are used and evaluated to study their impact on annual revenues of a concentrated solar power plant (CSP). Other works, such as (Minis et al., 2019), use photovoltaic (PV) panels as local insolation sensors combined with a few more fixed ones to obtain a spatial DNI measurement. A method based on sky imaging is described in (Quesada-Ruiz et al., 2014) to forecast the intra-hour DNI. Cameras have been used to detect shadows and generate irradiance map, as in (Kuhn et al., 2017). Despite many of these methods depend on sensors fixed to the ground or at the top of buildings like towers, they can be used with the alternative presented in this work to improve the results combining their data.

In recent years, the significant development of unmanned aerial vehicles (UAVs) and their characteristics, such as their manoeuvrability, reduced dimensions, capacity for using different devices (a wide range of sensors, cameras, or more specific tools, such as fumigation sprayers), speed, along with others, has allowed their use in various applications. Beyond military purposes, they have been used in fields such as agriculture (Rokhmana, 2015), area surveillance (Gu et al., 2018), as a camera tool for the film industry (Mademlis et al., 2019), or for safety and rescue tasks (Silvagni et al., 2017), among others. They have also been used in PV solar plants to inspect and monitor operations through thermal and visual cameras (Quater et al., 2014; Grimaccia et al., 2015).

This paper presents a mobile sensor system to detect and estimate DNI in areas with low DNI values due to the effect of clouds shadows. This work makes use of a multi-UAV system or a team of UAVs equipped with lightweight, cheap, low energy consumption sensors to measure DNI to locate and characterise the shadow of moving clouds, both its dimensions and its sun-blocking characteristics. The proposed algorithm is tested and discussed in simulations. The sun-blocking characteristics of the clouds shadow are modelled with a sigmoid-based function, which parameters are computed using the measurements taken by the UAVs. In summary, the main contributions are to provide an estimation of the drop of DNI caused by the effects of clouds shadows based on measurements, after locate and track the shadow, and how it affects the output temperature of a solar power plant.

The paper is organised as follows. Section 2 describes the problem under consideration. Section 3 presents the proposed solution, tested by simulations in Section 4. Finally, some conclusions and remarks are drawn in Section 5.

2. Problem overview

The objective of this work is to estimate the DNI in the area of a solar power plant in presence of moving clouds. This paper is based on the work presented in (Aguilar-Lopez et al., 2021) to locate and characterised the shape of a shadow of a static cloud.

A set of $U = \{u_1, u_2, ..., u_{nu}\}$ UAVs is deployed to achieve this task, equipped with lightweight low-energy consumption sensors to measure DNI (Solar Mems Technologies, 2019), as the shown in Figure 1. UAVs are assumed to move at a constant average speed based on commercial UAVs as *DJI Phantom 3* (DJI Technology Inc., 2015). The control architecture of the multi-UAVs system is a centralised topology: all UAVs send their state and measurements to a ground station computer. This ground station makes computations and commands new actions. To avoid collisions between the UAVs, each one flies 5 meters higher over the previous one.

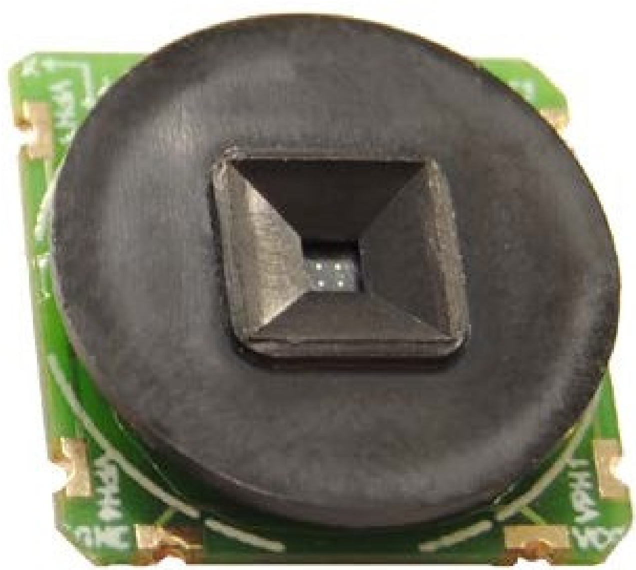

Figure 1: NANO-ISSX sun sensor from Solar Mems.

The moving clouds are assumed to project an elliptical shadow C over the ground as a result of their sun-blocking characteristics over the DNI. Clouds velocity is computed from the wind speed and direction, which are known at ground level and adjusted to clouds level by using cameras looking both at the sky and the projected cloud shadow. The sun-blocking characteristics are modelled as a sigmoid function (see Figure 2a) that assigns a reduction factor over clear-sky DNI to every position under the influence of the shadow depending on the distance to the ellipse centre (see Appendix A for more details). The reduction factor is in the range $[0, 1]$, being 1 a clear-sky irradiance and 0 when the position receives no DNI. An example of the DNI losses due to clouds is depicted in Figure 2b.

3. Proposed solution

The solution proposed is divided into three stages:

1. **The search of the clouds shadow:** the objective of this stage is to locate positions with low values of DNI in the area of interest, i.e., to find the clouds shadow. A covering area problem is solved through an hybrid algorithm. This stage is described in Subsection 3.1.
2. **The characterization of the clouds shadow:** in this stage the UAVs take measurements of the clouds shadow. These measurements are used to create a polytope envelope to estimate the parameters of the elliptical shape, and also with a non-linear least squares method to estimate the DNI distribution. This stage is explained in Subsection 3.2.
3. **The follow-up of the clouds shadow:** the last stage is to track the clouds shadow while it affects the solar plant performance. As the shadow moves, an adjustment of past measurements is made with the wind data. This procedure is detailed in Subsection 3.3.

3.1. Hybrid algorithm

The algorithm has three parts: the extension of the field, the ACO inspired motion, and the Boustrophedon motion. They are briefly commented below.

Extended field for searching and area decomposition

The UAVs search low DNI points in an auxiliary region A around the solar field to locate and characterize the shadow C before it enters the solar field. As the wind speed and direction are known, the clouds shadow approached direction is inferred from them, so A does not have to be significantly large

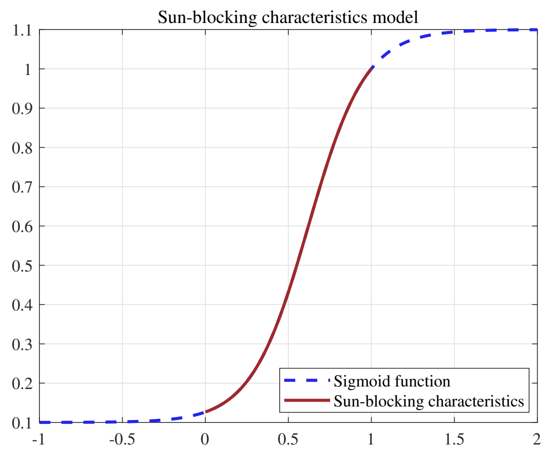

(a) Sigmoid.

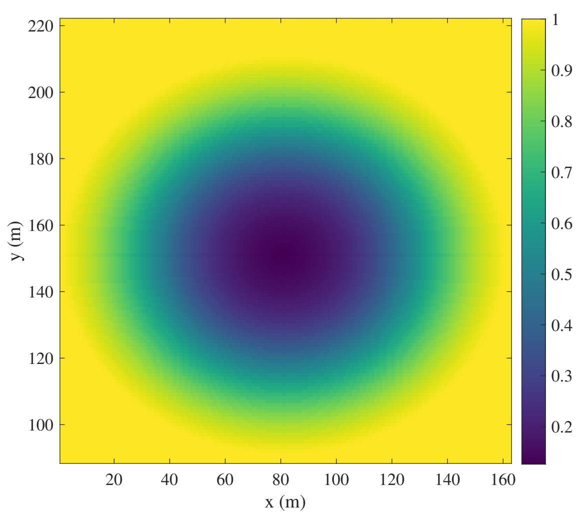

(b) DNI losses due to clouds.

Figure 2: Clouds sun-blocking characteristics.

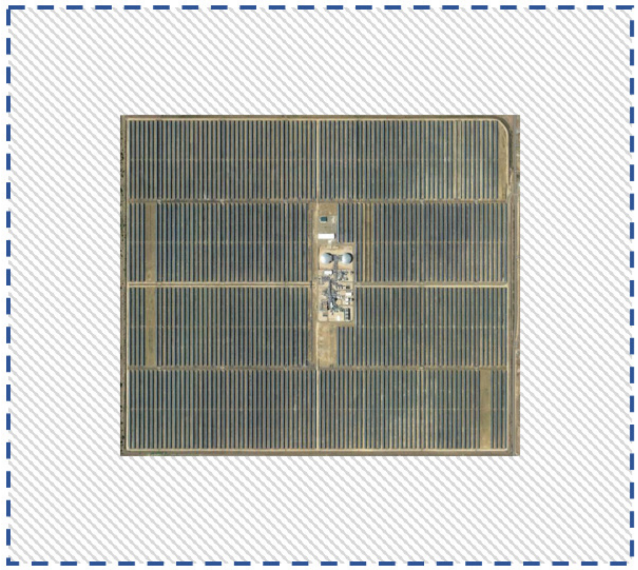

Figure 3: Overview of the auxiliary region for searching the clouds shadow, represented by the dashed line and the striped background. The Extresol-I power plant (ACS/Cobra Group, 2010) is used here as an example.

and the UAVs do the search in the portion of A where the clouds come into the field. Figure 3 shows an example of this auxiliary region A.

The hybrid algorithm decomposes the area into two layers which are explored differently. This first layer is a grid of N rows and M columns, and it is inspected with an algorithm inspired by the ACO algorithm, detailed in Subsection 3.1. The second layer is a decomposition of each one of the $N \times M$ cells of the first layer into a grid of $r \times c$ meters, where the DNI measurements taken by the UAVs are stored, and it is explored with a Boustrophedon motion explained in Subsection 3.1.

Summarising, the algorithm is two-steps: first, the UAV chooses a cell i from the $N \times M$ grid, through the ACO-inspired algorithm. Once the UAV reaches that cell, a sweep of the area is made with a Boustrophedon motion. After that, the algorithm starts again with the first step.

UAVs are continuously taking irradiance measurements, $I(x)$, at their positions, x. This seeking mode continues until any UAV detects a low DNI measurement, $I(x) < I_{th}$, being I_{th} a threshold value based on the clear-sky irradiance.

ACO inspired algorithm

The original ACO algorithm deploys numerous *virtual ants* to connect the starting node with the destination node. These ants travel along the nodes of the optimisation problem to conform possible solutions. After evaluate the solutions with a cost function, ants drop an amount of *pheromones* in the nodes directly proportional to the quality of their solution. This way, iteration after iteration, the nodes with more *pheromones* are more likely to be chosen, and the best solution is found.

In the ACO inspired algorithm, the UAVs are the *virtual ants*, the cells of the first layer are the nodes and instead of *pheromones* the UAVs drop *repellent*. The *repellent* works contrary to *pheromones*: the more *repellent* a cell has, the less probable it is to be visited. This way, UAVs travel cell after cell of the first layer in a probabilistic manner, generally avoiding the already visited ones, though repetition is permitted as new clouds can come in after a while. The probability to choose a cell by the *repellent* on it is expressed as (1):

$$p_{ij}^{\tau} = 1 - \frac{\tau_{ij}}{\sum_k^N \sum_l^M \tau_{kl}}, \tag{1}$$

where τ_{ij} is the amount of *repellent* on the cell ij.

Additionally, to achieve an efficient coverage, UAVs should avoid each other to explore different regions of the area. The probability of visiting a cell taking into account this consideration is defined as:

$$p_{ij}^{d} = \frac{d_{ij}}{\sum_k^N \sum_l^M d_{kl}}, \tag{2}$$

where d_{ij} is the distance between the position of the UAV to avoid and the cell ij. The final probability to choose a cell is obtained with (3).

$$p_{ij} = \frac{p_{ij}^{\tau} p_{ij}^{d}}{\sum_k^N \sum_l^M p_{kl}^{\tau} p_{kl}^{d}}. \tag{3}$$

Boustrophedon motion

The Boustrophedon motion creates a back and forth path to cover the second layer. It is important to remark that not every cell of the second layer is inspected: this would be inefficient because very small cloud shadows do not affect the plant behaviour significantly. A minimum wide of the corridor for the Boustrophedon motion is pre-settled to sweep the area and find the shadows of interest in a short time. Figure 4a depicts the ACO inspired algorithm and the Boustrophedon motion.

Remark. As the communication with the ground station is constant, any possible failure of any UAV in completing its task is assumed to be noticed and compensated by the ground station with the remaining UAVs.

3.2. Clouds shadow characterisation

This stage is divided into two phases: the objective of the first phase is to delimit the contour of the shadow, and the objective of the second phase is to estimate the parameters of the ellipse and the irradiance distribution.

Measuring the DNI

Once a location with a DNI value under the threshold I_{th} is detected, all UAVs are called to take measurements of the region. The first step is to describe the border of the shadow to get an approximation of its size, and the second step is to take samples of the inner DNI to get a proper distribution of the DNI.

$$K_X = \begin{pmatrix} -1 & 0 & 1 \\ -2 & 0 & 2 \\ -1 & 0 & 1 \end{pmatrix}, \tag{4a}$$

$$K_Y = \begin{pmatrix} 1 & 2 & 1 \\ 0 & 0 & 0 \\ -1 & -2 & -1 \end{pmatrix}. \tag{4b}$$

The UAVs compute an irradiance gradient to follow the perpendicular vector to it, i.e., the irradiance isoline, and take measurements of the border. When an UAV comes to the region with low DNI values, it does an initial inspection following a *quadratic spiral path*, see Figure 4b. Using the measurements taken in this path, an irradiance map I_{map} is created, and then it is convolved with the kernels of the *Sobel operator*, see (4a) and (4b), to get the discrete approximation of the derivatives in each position, see (5a) and (5b). The mean gradient of I_{map} is used as the searched irradiance gradient.

$$I_x = \frac{\delta I}{\delta x} = K_X * I, \qquad I_y = \frac{\delta I}{\delta y} = K_Y * I, \tag{5a}$$

$$\nabla I = \begin{bmatrix} I_x \\ I_y \end{bmatrix}. \tag{5b}$$

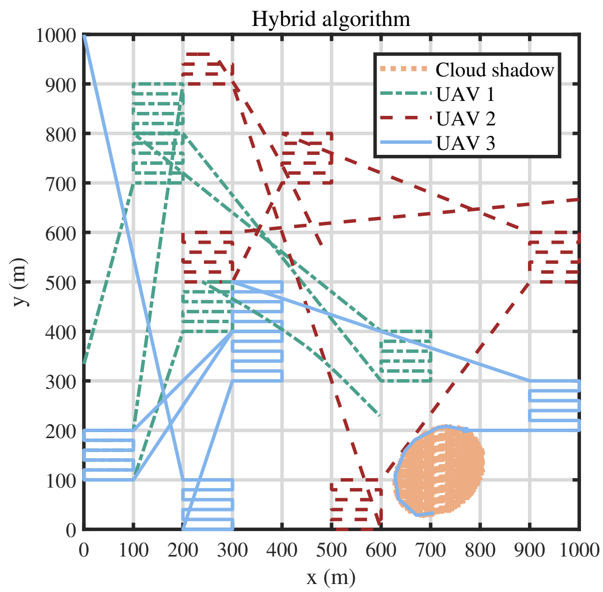

(a) Hybrid algorithm example of searching.

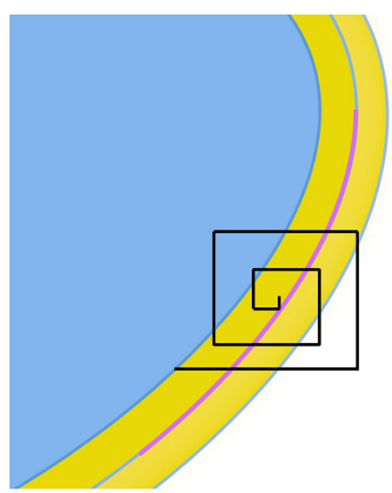

(b) Quadratic spiral example.

Figure 4: Examples of the employed motions in this work. In the hybrid algorithm ACO inspired motion is used among cells and Boustrophedon motion inside a cell, meanwhile quadratic spiral is used for measuring in the shadow contour.

The direction of the irradiance isoline is computed and the UAVs follow it taking DNI measurements. For a proper DNI distribution estimation, when two or more UAVs are in the cloud shadow region, one of them follows the irradiance gradient instead of the isoline to take inner DNI measurements.

Estimation of the shape of the shadow

Polytope envelope.

The estimated shape of the shadow is characterised by a polytope. This polytope is defined by the convex hull of the positions with a solar irradiance value under the threshold I_{th}.

The inequation (6) defines the polytope Q:

$$Hx \leqslant K, \tag{6}$$

where $H \in \mathbb{R}^{n\times m}$, $K \in \mathbb{R}^n$ and $x \in \mathbb{R}^m$, being n the number of restrictions that defines the region of the polytope and m the coordinates dimension. As the shadow is a projection over the ground, $m = 2$. If any point x satisfies the inequation (6), then $x \in Q$, otherwise $x \notin Q$.

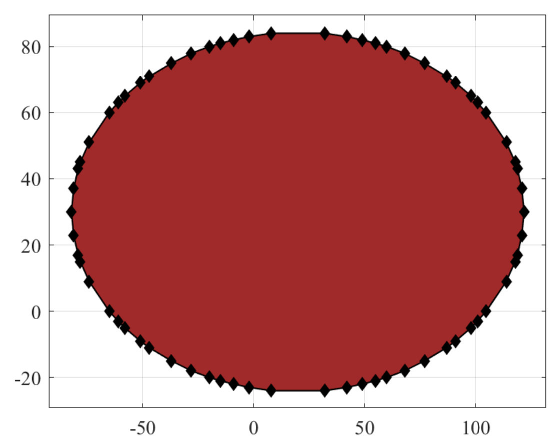

Figure 5: Polytope envelope.

As it was mentioned before, the UAVs explore the area looking for locations with irradiance values under I_{th}. When the UAVs find at least three points $x/\ I(x) < I_{th}$, the clouds shadow polytope Q_c is defined by the vertices set $V = \{x_1, x_2, x_3\}$. Successive positions $x_i/\ I(x_i) < I_{th}$ are evaluated with (6) defined for Q_c, and if $x_i \notin Q_c$, it is included in the vertices set

$V = \{x_1, x_2, ..., x_n\}$ and the polytope Q_c is redefined. The cloud shadow polytope Q_c envelope or convex hull, as depicted in Figure 5, is computed with the polytope class of the MATLAB Multi-Parametric Toolbox (Herceg et al., 2013).

Convex hull conversion to ellipse.
Q_c convex hull is used to obtain the parameters of the elliptical shape approximation of the shadow. These parameters are: the centre O_ϵ^{est}, the semi-major axis a^{est}, the semi-minor axis b^{est}, and the rotation angle θ^{est}. An ad-hoc purely geometrical heuristic method to compute these parameters is proposed and compared with two algorithms of the literature: one that solves the inner Löwner-John ellipsoid (Zhang, 2020), named here as the *internal* method; and another one that solves the outer Löwner-John ellipsoid (Li, 2020), denoted here as the *external* method.

The Löwner-John ellipsoids (Henk, 2012) are the maximum volume ellipsoid inscribed in a polytope and the minimum volume ellipsoid circumscribed about a polytope. These ellipsoids are computed by the *internal* and the *external* methods mentioned above . Let Q be a polytope defined as (6), and let ε be the ellipsoid defined as (7):

$$\varepsilon(O_\varepsilon, E) = \{\ x \mid x = E\mu + O_\varepsilon,\ \mu \in \mathbb{R}^m,\ \ \| \mu \| \leq 1\}, \tag{7}$$

where $\| \cdot \|$ is the euclidean norm, O_ε the centre of the ellipsoid and E a positive definite symmetric matrix $m \times m$. Being ν the volume of the m-dimensional unit ball, the volume of the ellipsoid ε is:

$$\mathrm{Vol}_\varepsilon = \nu \ \det(E). \tag{8}$$

Thus, the Löwner-John minimum volume ellipsoid circumscribed problem can be written as (9).

$$\begin{aligned} \min \quad & -\log \det(E), \\ \text{s.t.} \quad & K - HE\mu - HO_\varepsilon \geq 0, \\ & E \geq 0. \end{aligned} \tag{9}$$

For the inner Löwner-John ellipsoid, let ε' be the ellipsoid defined as (10) and the polytope Q' be defined by its vertices set $Q' = \{x_1, x_2, \ldots, x_n\}$. The maximum volume ellipsoid inscribed problem can be written as (11).

$$\varepsilon'(O_{\varepsilon'}, E') = \{\ x \mid \ \| E'(x - O_{\varepsilon'}) \| \leqslant 1\}, \tag{10}$$

$$
\begin{aligned}
\max \quad & \det(E'), \\
\text{s.t.} \quad & \| E'(x_i - O_{\varepsilon'}) \| \leqslant 1, \\
& E' \geq 0.
\end{aligned} \tag{11}
$$

Both problems are solved with the algorithms mentioned above, which implement the works of (Khachiyan, 1996) and (Zhang and Gao, 2003). For the problem of this paper, the dimension of the ellipsoid is 2, i.e., an ellipse.

Our ad-hoc heuristic method is based on geometric operations. First, it computes the estimated centre O_{ε}^{est} of the ellipse as:

$$
O_{\varepsilon}^{est} = \frac{\sum_{i=1}^{N_V} x_i}{N_V}, \tag{12}
$$

where x_i are the N_V vertices of the polytope Q_c. Then, the distance between every vertex and this estimated centre is computed with the Euclidean norm. The nearest vertex to the centre is $x_{nearest}$. It is defined the straight line $line_1$ between the estimated centre and $x_{nearest}$. To find the cut points between $line_1$ and the polytope envelope, a set of candidate points $x_{candidate\ points}$ is computed as show (13a) and (13b), where a point is defined as $x = (\chi_1, \chi_2)$.

$$
line_1 \equiv \chi_2 = q_1\chi_1 + q_2, \quad H \begin{bmatrix} \chi_1 \\ \chi_2 \end{bmatrix} = \begin{bmatrix} h_{11} & h_{12} \\ h_{21} & h_{22} \end{bmatrix} \begin{bmatrix} \chi_1 \\ q_1\chi_1 + q_2 \end{bmatrix} = \begin{bmatrix} k_1 \\ k_2 \end{bmatrix} = K, \tag{13a}
$$

$$
x_{\text{candidate points}} = (\chi_1, \chi_2) = \left(\frac{k_i - h_{i2}\ q_2}{h_{i1} + h_{i2}\ q_1}, \quad q_1 \frac{k_i - h_{i2}\ q_2}{h_{i1} + h_{i2}\ q_1} + q_2 \right). \tag{13b}
$$

Evaluating $x_{candidate\ points}$ with (6) as strict equality (14) the two cut points $x_{cut\ points}$ are found as they are the only ones that fulfil all restrictions.

$$
H_{Q_c} x_{\text{cut points}} = K_{Q_c}. \tag{14}
$$

The estimated centre O_{ε}^{est} is adjusted being the middle point between these $x_{cut\ points}$. The process is repeated but searching the farthest point $x_{farthest}$, that defines the line $line_2$ with O_{ε}^{est}. To estimate the semi-major axis, a group of lines is defined rotating $line_2$ around O_{ε}^{est} a couple of degrees. The cut points between these lines and the polytope envelope define another set of points, and the two farthest among are called x_{a1} and x_{a2}. Half the distance between x_{a1} and x_{a2} is the estimated semi-major axis a^{est}. The estimated semi-minor axis b^{est} is computed identically but rotating $line_1$ around O_ε^{est}.

Finally, the estimated rotation angle of the ellipse θ_ε^{est} is found as the angle between the x-axis and the vector that connects x_{a1} and x_{a2}, as shows (15).

$$\overrightarrow{x_{a1}x_{a2}} = (\chi_{1v}, \chi_{2v}), \quad \theta^{est} = \arctan \frac{\chi_{2v}}{\chi_{1v}}. \tag{15}$$

Sun-blocking characteristics.

As it was mentioned in Subsection 3.2, to determine the sun-blocking characteristics of the clouds shadow, one of the UAVs takes irradiance measurements while travelling along the irradiance gradient direction in the downward sense.

Using these irradiance measurements, a model of the cloud sun-blocking characteristics is computed with a variation of the sigmoid function, given in (16):

$$f(\delta) = \frac{1}{1 + e^{a_\sigma \delta + b_\sigma}} + c_\sigma, \tag{16}$$

where parameters a_σ, b_σ and c_σ determine the inflection point, slope, and the offset. This function gives the sun-blocking characteristics of a position x_i depending on its normalised distance to the centre of the ellipse, as it was explained in Section 2, and more detailed in Appendix A. The sun-blocking characteristics of any position in the cloud obtained this way resulting in a function as depicted in Figure 2.

To determine the values of a_σ, b_σ and c_σ a non-linear least squares problem is solved. The measurements conform an array of pair values (δ_i, I_i), where I_i is the irradiance value of a position at a normalised distance δ_i. (17) shows the problem.

$$\min_{a_\sigma, b_\sigma, c_\sigma} \sum_i [F(a_\sigma, b_\sigma, c_\sigma, \delta_i) - I_i]^2. \tag{17}$$

The initial solution $(a_{\sigma0}, b_{\sigma0}, c_{\sigma0})$ is computed through an equation system, so three points are needed. Two of them are the maximum irradiance value, corresponding to the maximum distance inside the ellipse, i.e., the semi-major axis, $\delta = a$, and the minimum irradiance value, corresponding to the minimum distance, $\delta = 0$. The last one is the most interesting point between the maximum and the minimum, that is, the point where the sigmoid changes its tendency and starts to grow fast. This point is the one with the maximum value of the second derivative, computed with the discrete expression (18), where s is the discrete step.

$$f''(\delta_0) \approx \frac{f(\delta_0 + s) - 2f(\delta_0) + f(\delta_0 - s)}{s^2}. \tag{18}$$

3.3. Following the clouds shadow

In contrast to the problem in (Aguilar-Lopez et al., 2021), now the cloud shadow is non-static, and the same shadow point can be measured more than once in various locations according to the shadow motion. The proposed solution is to adapt the past shadow polytope points, x_i as shows (19), assuming the speed of the shadow $\overrightarrow{V_C}$ can be estimated from the wind:

$$x_t = x_0 + (t - t_0) \cdot \overrightarrow{V_C}, \tag{19}$$

being x_t the point adapted to instant t and x_0 the point at instant t_0.

4. Simulations results

This section is divided into two parts. In the first one, simulation results about the performance of the proposed algorithm are depicted. In the second part, the effects of the clouds shadow over a power plant are shown.

4.1. Results of clouds shadow detection and description

The developed work to estimate the effects of the shadow of moving clouds in the DNI has been tested in two scenarios. In both cases, the extended area A and the layout of the solar plant size together 2130 m $\times$ 1300 m, see Figure 3. The grid decomposition of the ACO-inspired algorithm is of 10×10 cells. We have assumed that the minimum size of a cloud shadow that affects the solar plant efficiency is 20 m for the minor semi-axis, so the wide of the corridor of the Boustrophedon motion is set to that value. To locate and characterise the shadow 6 UAVs are commanding by the ground station computer. UAVs are assumed to have neither restrictions in movement nor energy, keeping an average constant speed of 8 m/s at any given time. See Conclusions Section for some comments about these asumptions. As mentioned before in Section 2, this speed is based on a commercial UAV (DJI

Technology Inc., 2015). Their initial positions are equidistant around the perimeter of the area to surveil.

Each case simulates a different day. Table 1 shows the parameters of the cloud shadow in each case. The DNI over the clouds for both simulations is of 750 W/m^2, and the irradiance threshold I_{th} is a 97% of the DNI to avoid considering a shadowless point as a cloud shadow point.

Table 1: Cloud shadow parameters of both simulations.

Parameter	**First cloud shadow**	**Second cloud shadow**
Semi-major axis (m)	75	75
Semi-minor axis (m)	45	60
Rotation angle (°)	30	45
Movement direction $\overrightarrow{s} = (s_x, s_y)$	$(1, 0)$	$(3, -1)$
Speed (m/s)	1	1

The estimation results of the parameters of the shape of the shadow are depicted in Figures 6 and 7. Figures 8 and 9 show the estimated irradiance map. The first portion of the cloud shadow came into the area A after 25 seconds. The UAVs found the shadow after 129 seconds, and they estimated its shape and sun-blocking characteristics completely after another 50 seconds. As a reference, the cloud shadow reaches the plant layout at second 325. In Subsection 3.2 it was explained that UAVs take irradiance measurements of the inner region of the cloud shadow. These measurements are used to compute the irradiance function distribution and obtain a proper estimation of the DNI in the area. Until the UAV responsible for taking the measurements has not finished this task, the cloud shadow region is assumed to have constant sun-blocking characteristics equal to the minimum irradiance value found.

The evolution of the mean error in the region affected by the cloud shadow depending on the number of UAVs flying over the area is depicted in Figure 10. There is a significant difference in the time to find and describe the cloud shadow between a team of 3 UAVs and one of 6 UAVs, but this difference is less significant between the 6-UAVs team and the 12-UAVs team.

Results of the second case are very similar and are shown in Figures 11 and 12. The evolution of the error for this case is depicted in Figure 13. In both simulation cases, the mean error is approximately of 15-20 W/m^2.

To compare the three methods proposed in Subsection 3.2, the measurements of the first simulation were computed with the three of them. Table

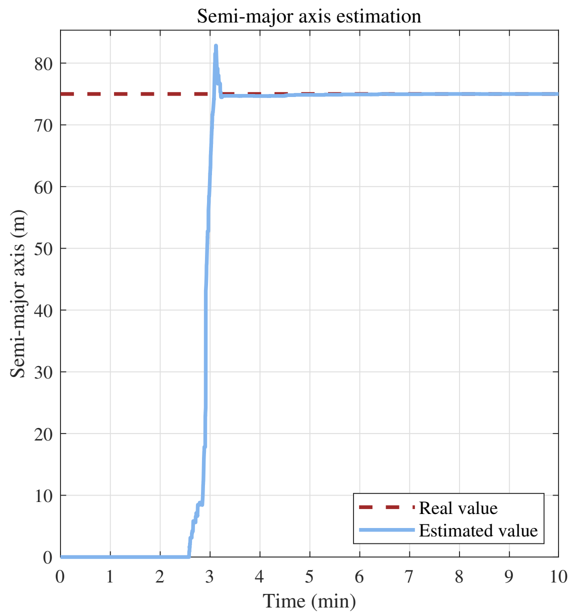

(a) Semi-major axis estimation.

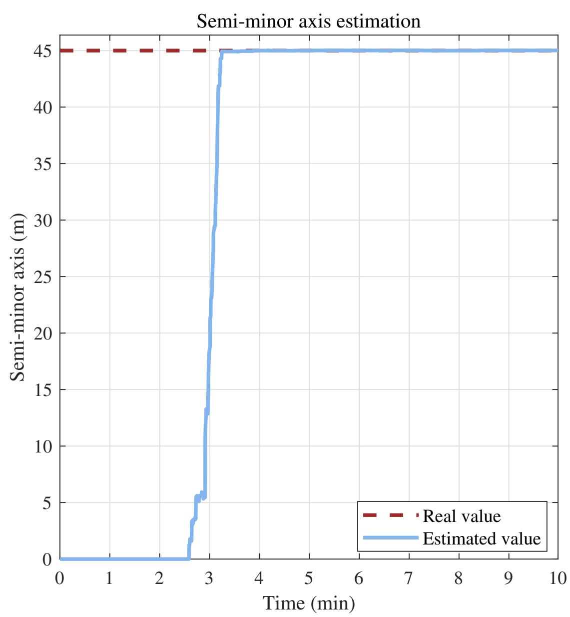

(b) Semi-minor axis estimation.

Figure 6: Semi-axes estimated size of the elliptical shape in the first simulation case.

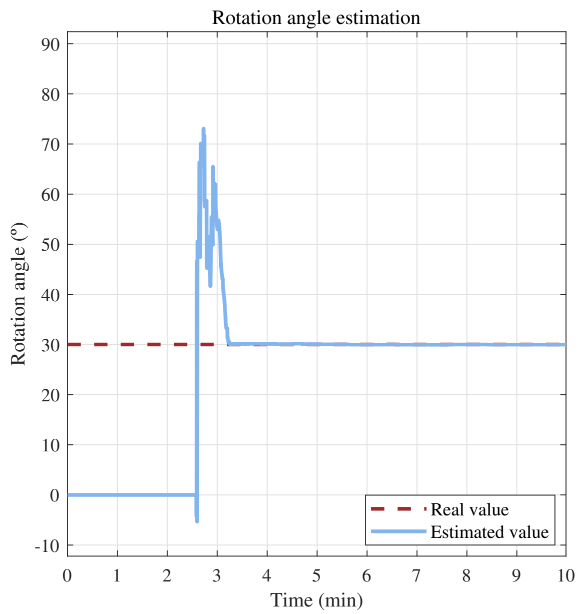

(a) Rotation angle estimation.

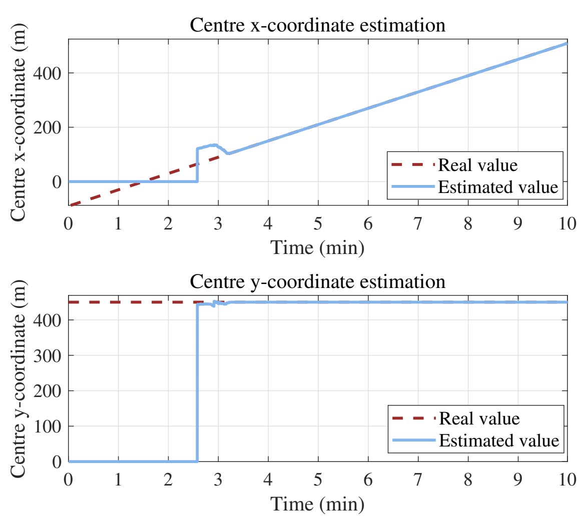

(b) Centre location estimation.

Figure 7: Estimated rotation angle and centre of the elliptical shape in the first simulation case.

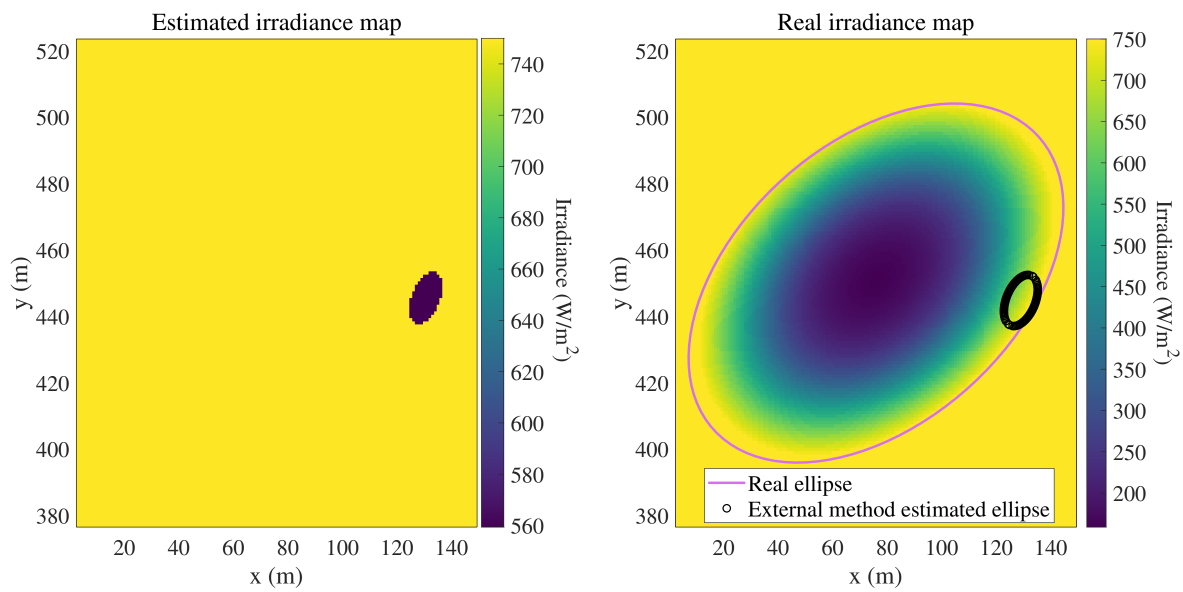

(a) 10 seconds after the cloud is found.

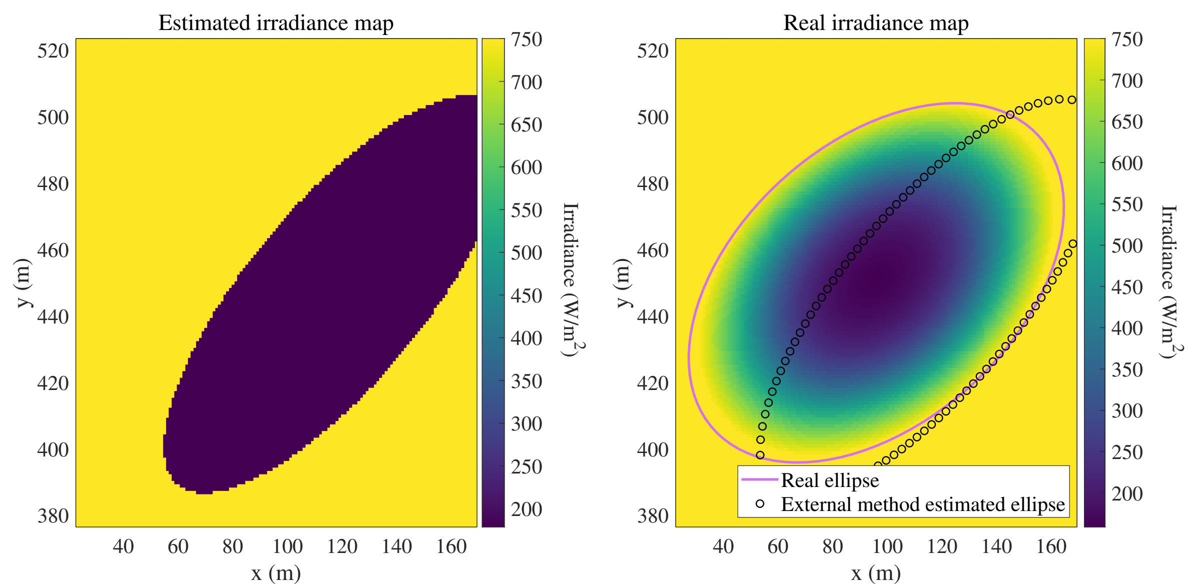

(b) 30 seconds after the cloud is found.

Figure 8: Initial and intermediate estimated irradiance map and estimated elliptical shape of the shadow.

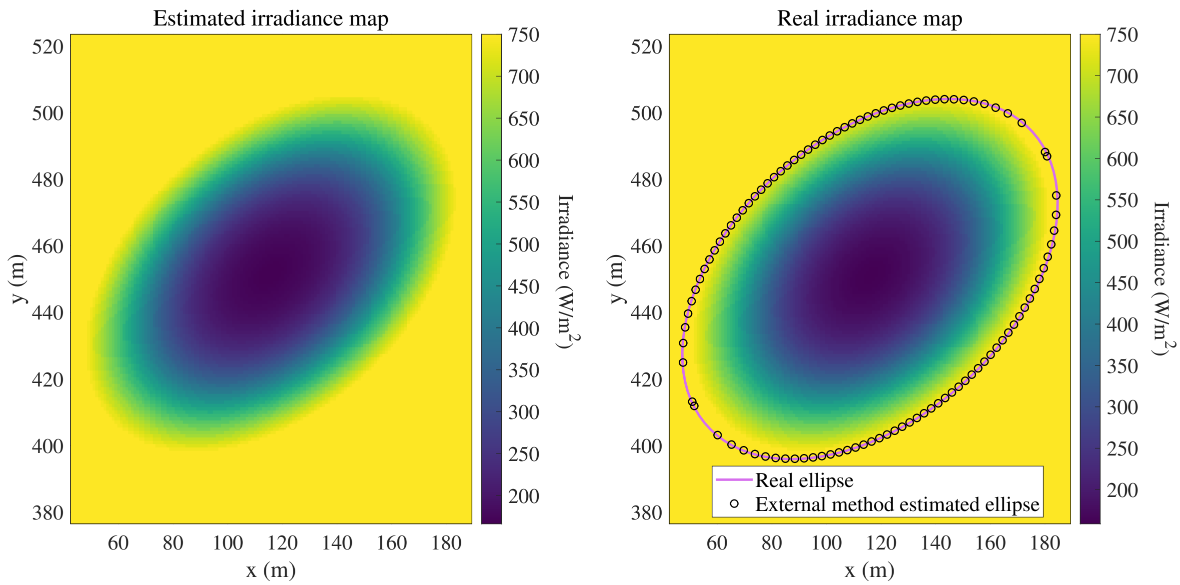

Figure 9: 50 seconds after the cloud is found the final estimated irradiance map and the estimated elliptical shape of the shadow are obtained.

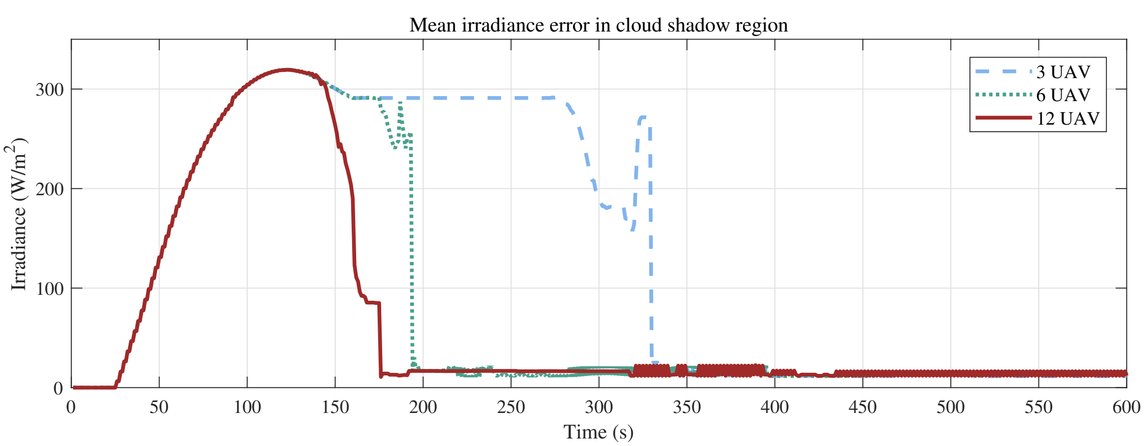

Figure 10: Mean irradiance error in the region affected by the cloud shadow in the first simulation case.

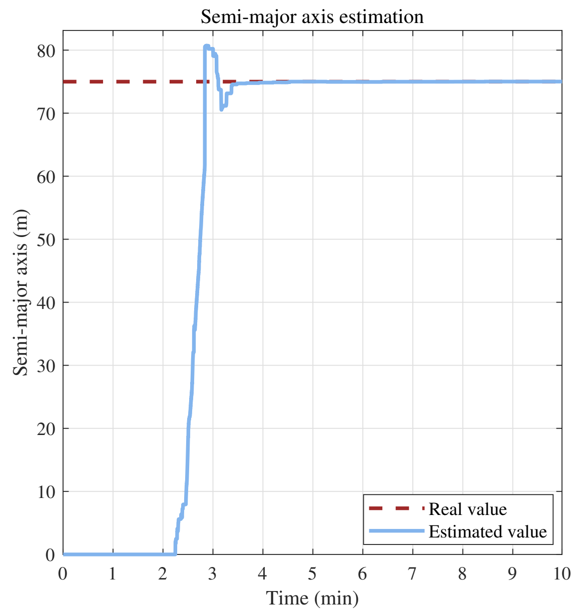

(a) Semi-major axis estimation.

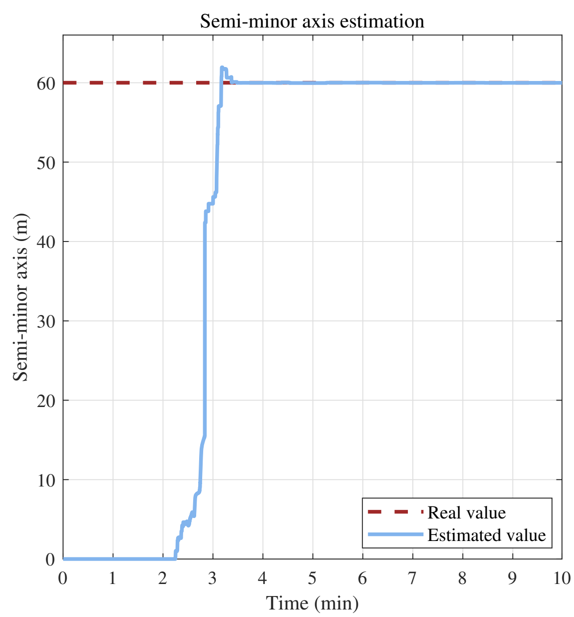

(b) Semi-minor axis estimation.

Figure 11: Semi-axes estimated size of the elliptical shape in the second simulation case.

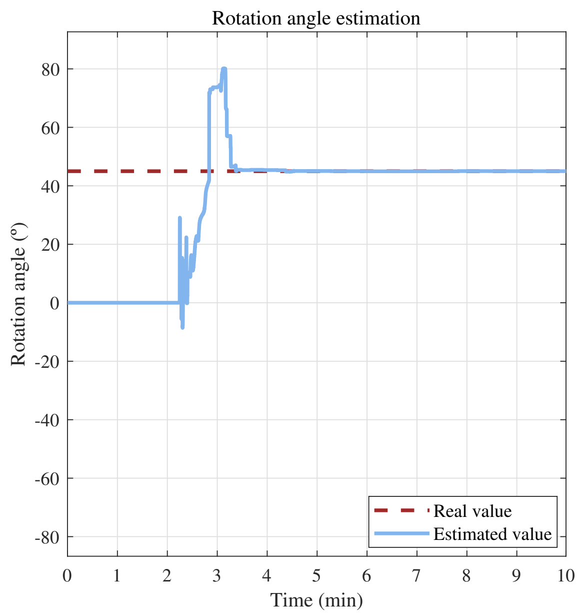

(a) Rotation angle estimation.

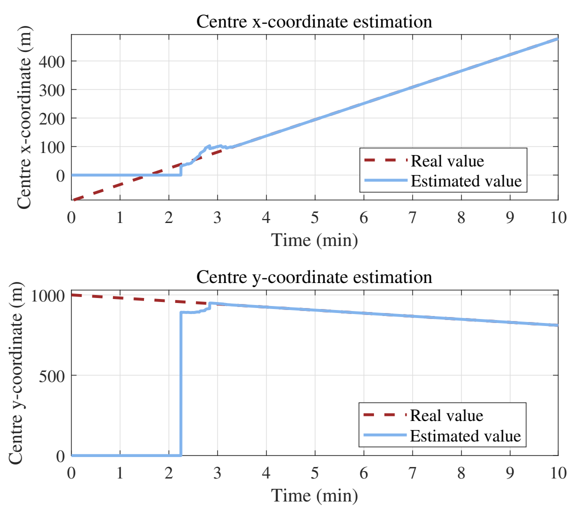

(b) Centre location estimation.

Figure 12: Estimated rotation angle and centre of the elliptical shape in the second simulation case.

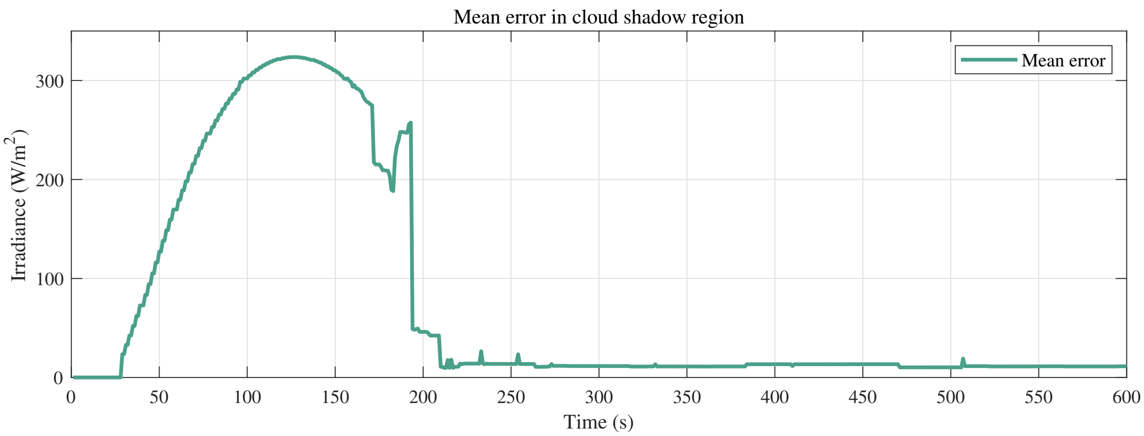

Figure 13: Mean error in the region affected by the cloud shadow in the second simulation case.

2 shows the results. The *external* method is the best one, though the others got estimation near the real value.

To study the computational time cost of every method, another type of simulation has been done. Twelve sets of 1000 randomly generated ellipses have been created. Each set differs from the others in the number of points that define each ellipse: the first set contains ellipses defined by 25 points, the second one ellipses defined by 50 points, and this progression continues up to 300 points. An example of these randomly generated ellipses is depicted in Figure 14a. This test aims to measure how much time each method takes to compute the ellipse properties and check if the number of points that defines the ellipses affects the results. Figure 14b and Table 3 expose the results. The *external* ellipse algorithm is the slowest one, while the ad-hoc heuristic is the fastest one. The reason for the better computational time performance of the ad-hoc heuristic method is that, while the other ones have to compute operations as inverse matrices, the proposed one only uses simpler operations as multiplications. Finally, the number of points that define the ellipses makes the methods take more computation time but do not change which one is the slowest or fastest one. To summarise, the proposed ad-hoc algorithm has the less computational time result with similar estimation to the *external* method, making it preferable to use with less computational capable systems.

Table 2: First simulation case results. The final ellipse parameters estimation and their oscillations are shown.

	Real value	Ad-hoc	External	Internal
Semi-major axis (m)	75	74.46 ± 0.21	74.92 ± 0.11	72.92 ± 0.76
Semi-minor axis (m)	45	44.79 ± 0.10	45.01 ± 0.01	43.52 ± 0.23
Rotation angle (°)	30	31.09 ± 1.23	30.01 ± 0.05	24.65 ± 0.25
Centre x-coordinate deviation (m)	-	1.13 ± 0.53	0.07 ± 0.03	0.19 ± 0.49
Centre y-coordinate deviation (m)	-	1.41 ± 0.66	0.02 ± 0.01	0.01 ± 0.15

Table 3: Computational time test results

Method	Time (s)	Method time/Ad-hoc time
Ad-hoc	$2.24 \cdot 10^{-4} \pm 1.54 \cdot 10^{-4}$	1
External	$2.71 \cdot 10^{-3} \pm 4.72 \cdot 10^{-4}$	12.10
Internal	$9.71 \cdot 10^{-4} \pm 2.10 \cdot 10^{-4}$	4.33

4.2. Clouds shadow effects simulation

In this section, simulations of two cases of isolated clouds passing through the field on two different summer days with medium radiation are presented. Both clouds are equal in size to the detected in the previous section, but with a slower motion since this increases their effect on the solar plant. The simulated effect of the clouds on the solar field is exposed. The plant model used is a 50 MW plant with 90 loops (Sánchez et al., 2019), with an approximate length of 600 m each. Every loop is divided into two rows of 300 m each (row 1: collectors 1 and 2, row 2: collectors 3 and 4) with an approximate separation of 17 m between the rows of mirrors (Montes et al., 2009).

The simulated field structure is composed of an upper and a lower solar field with 45 loops each and the steam stage located in the centre, see Figure 15. The approximate length of each solar field is approximately 1530 m, while the width of each field corresponds to the length of the two collectors, namely, 300 m. For these simulations, the control strategies for solar field temperature tracking and defocusing using generalised predictive controllers (GPCs) presented in (Sánchez et al., 2018a) have been used, with a defocusing temperature set at 396 °C.

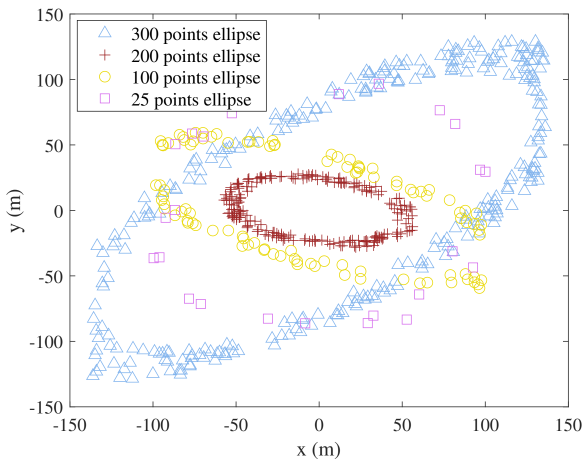

(a) Randomly generated ellipses of 25, 100, 200 and 300 points.

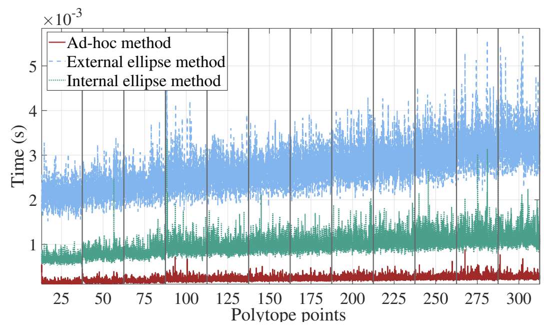

(b) Methods time cost.

Figure 14: Results of the computational time tests for the three methods to estimate an ellipse.

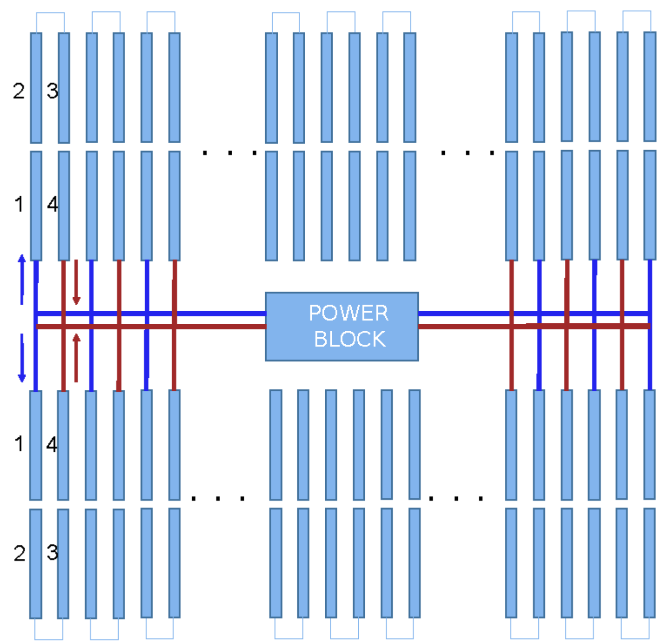

Figure 15: Solar field structure used for simulation

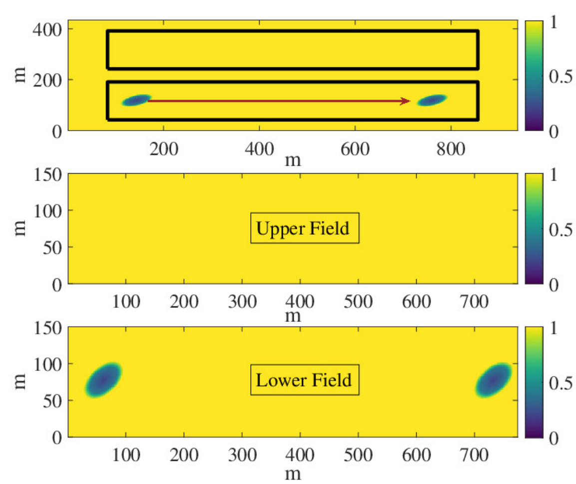

Figure 16: Horizontal Cloud (left to right). Speed = 0.2 m/s. Upper and Lower solar fields are marked with a black rectangle.

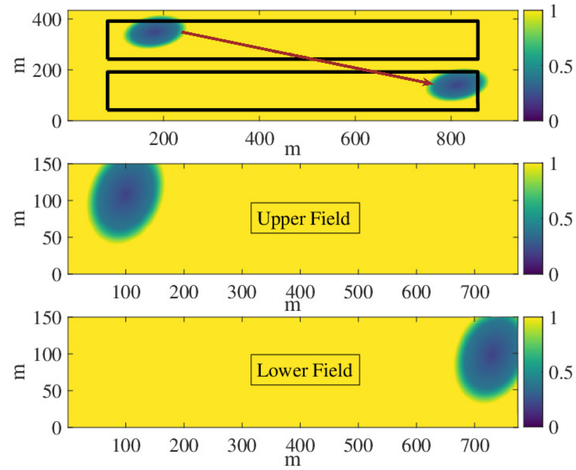

Figure 17: Diagonal Cloud (left to right). Speed = 0.2 m/s. Upper and Lower solar fields are marked with a black rectangle.

Figures 16 and 17 show the two clouds that have been simulated. Both have a speed of 0.2 m/s. The smaller one has 75 meters of semi-major axis, 45 meters of semi-minor axis, and a horizontal movement that only affects the lower field. The second and larger one, corresponding to another summer day, has 75 meters of semi-major axis, 60 meters of semi-minor axis, and a diagonal movement, affecting first the upper field and later the lower field.

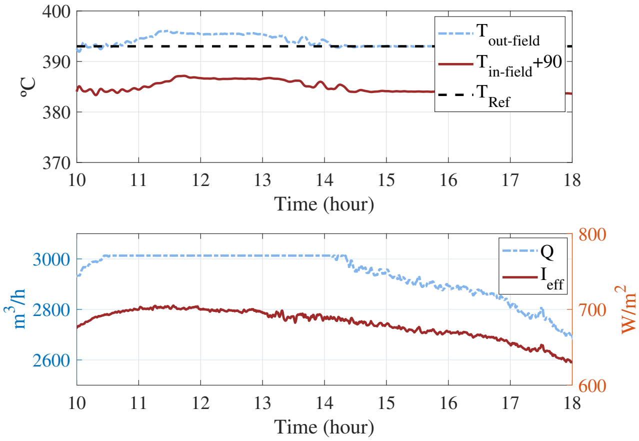

Figure 18: Horizontal Cloud (left to right). Speed = 0.2 m/s. Solar field temperatures, flow-rate and effective DNI.

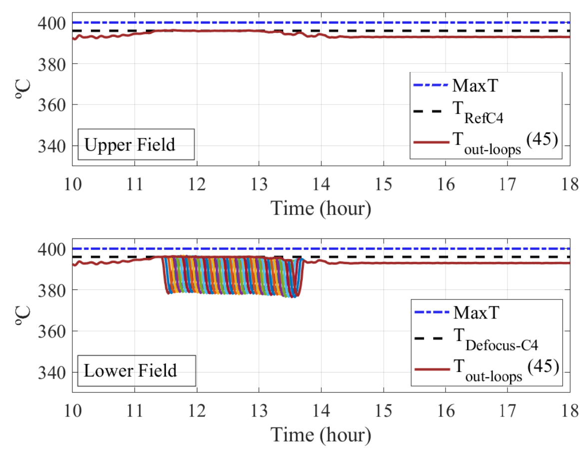

Figure 19: Horizontal Cloud (left to right). Speed = 0.2 m/s. Loops' temperatures, upper and lower fields.

In Figures 18 and 19 it can be seen how the small horizontal cloud affects only the lower solar field. However, since it is a small-sized cloud, the outlet temperature of the lower field loops affected does not suffer an excessively abrupt drop. Due to the small size of the cloud, only a small number of loops are subjected to the said cloud at any time instant. The simulations show the effective DNI, which includes the geometric efficiency, that is, $I_{eff} = I \cdot no$.

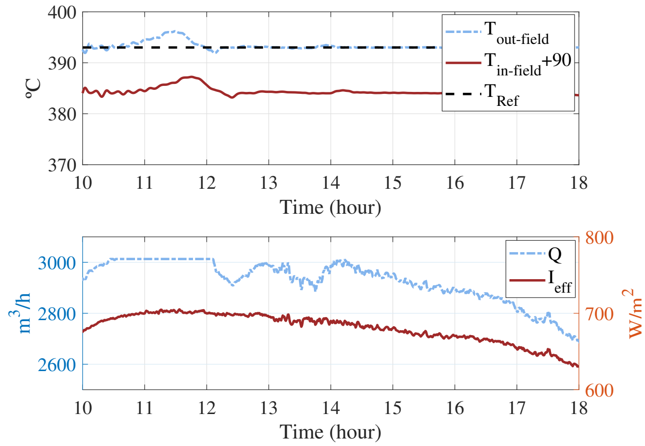

Figure 20: Diagonal Cloud (left to right). Speed = 0.2 m/s. Solar field temperatures, flow-rate and effective DNI.

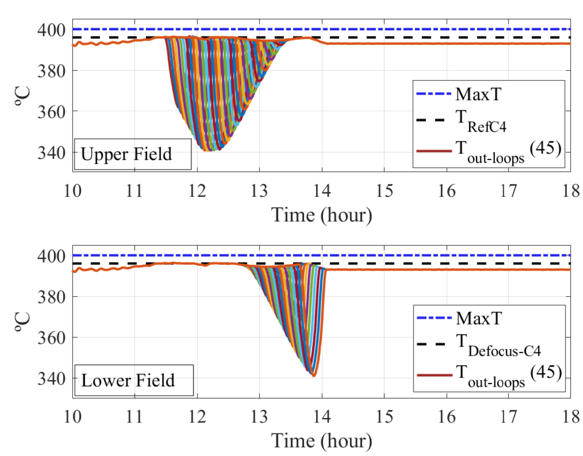

Figure 21: Diagonal Cloud (left to right). Speed = 0.2 m/s. Loops temperatures, upper and lower fields.

By increasing the size of the cloud, and diagonally, it can be seen how the effect on the loops is greater but also different because not all loops have the same area covered. This simulation is shown in Figures 20 and 21. In this case, the drop in temperature is more important, and this can be seen in Figure 21 and corroborated by looking at Figure 20 where, unlike the small horizontal cloud, now the flow has had to be decreased much earlier to maintain the nominal temperature set-point of the plant, 393 °C (Sánchez et al., 2018a). The problem with clouds is they cause the temperature drop off part of the solar field. This causes the field outlet temperature to drop, causing the flow controller to lower the flow-rate to maintain this temperature. This causes a portion of the field to heat up with the need to defocus when it might not be necessary. This effect may occur on days where the radiation is greater than that presented in these simulated scenarios. Other factors to also consider are the state of the loops, reflectivity, loop activated or deactivated, loop being cleaned, etc.

It is essential to have prior knowledge of the cloud as far as possible: its size, sun-blocking radiation characteristics, and speed. Very fast clouds barely affect the field, as well as very small clouds or clouds that pass only through a small portion of the field.

Given that each cloud affects the field differently, an effort should be made to analyse which types of clouds are the ones that should be estimated or not. This will enable us to make a proper adjustment of the plant and avoid defocusing parts of the field that are hotter than others where the cloud is passing, avoiding drops in flow-rate and, consequently, in electrical production. Besides, it is also necessary to include the possibility of lowering the field temperature set-point and operating, at least momentarily, at temperatures lower than nominal to maintain stable electrical production. This is especially desirable in renewable generation plants since a stable production is important to maintain the stability of the electrical network.

5. Conclusions

This paper has presented a multi-UAV system to locate and estimate regions with a low DNI value caused by the shadows of clouds. The UAVs take measurements of the irradiance values in the area of interest with cheap, lightweight, and low energy consumption sensors, and then the measurements are used to obtain an estimation of the shadow shape and its sun-blocking characteristics. The shape computation is made through three different methods tested by simulation and later discussed and compared. The sun-blocking characteristics function of the cloud is modelled as a sigmoid function, which parameters are estimated from the DNI measurements. Ultimately, the effects of two clouds detected by this method over a parabolic trough solar power plant are discussed by simulations.

The solution proposed has proved to locate and characterise the clouds shadow in the extended searching area A in approximately two minutes, before the shadow reaches the solar plant. The estimated irradiance map has a mean error of approximately 20 $\mathrm{W/m^2}$. About the three methods employed to compute the parameters of the ellipse approximation, the Löwner-John minimum volume ellipsoid circumscribed about a polytope method has been demonstrated to be the most accurate one, but also the slower one. The ad-hoc heuristic method proposed by the authors has shown to be the fastest one, with similar results of accuracy.

The simulations of the effects of the clouds shadow over a solar power plant showed that the temperature drop depends on the size, speed, and sun-blocking characteristics. The flow adjustment could lead to a heat-up of some parts of the solar field, with the need to defocus to avoid it. By knowing the characteristics of the incoming shadow, the defocusing and the consequent drop of electrical production can be prevented.

Plans for further research include modifying the algorithm to describe non-convex or non-elliptical cloud shadows or estimating the variable speed of the blast of wind. An important issue to address is the energy consumption of the UAVs depending on their path. Based on (Liu et al., 2017; Dorling et al., 2016), in this work we have assumed that the energy consumption is constant independently of the type of movement due to the low UAVs speeds, but future studies on energy optimal paths are needed. The analysis of which types of shadows are interesting is also an important question to tackle. Given that there are a limited number of UAVs with a limited operational flight time capacity, it is necessary to choose the cloud shadows that would be most interesting or important to estimate to make adjustments through advanced predictive controllers in the plant. In future works, the authors will analyse the cloud shadows to improve estimations and predictions through an optimal path planning strategy for UAVs. Another subject of study will be the use of control strategies as model predictive control to maintain the power production of the plant by using the information given by estimations and predictions.

Acknowledgements

The authors acknowledge the European Research Council (ERC) under the European Union's Horizon 2020 research and innovation programme for funding this work done under the advanced grant OCONTSOLAR, grant agreement No 789051.

Appendix A. Variable change for distance in the ellipse-circumference conversion

The reduction of the solar irradiance caused by C, namely, the sun-blocking characteristics of C, is modelled with a sigmoid function, such as the one depicted in Figure 2a. The domain of the sigmoid is $[0, 1]$ (blue segment) and it is dependent of δ, defined as (A.1).

$$\delta = \frac{\text{radius}_p}{\text{semi-major axis}}, \tag{A.1}$$

where $radius_p$ is computed through the circumference equation (A.2). This equation is derived from the rotated ellipse equation (A.3a) applying the transformation described in (A.3b) and depicted in Figure A.22, compound of a displacement, a rotation and a scale in the y coordinate.

$$x_2^2 + y_2^2 = \text{radius}_p^2, \tag{A.2}$$

$$\frac{[(x-x_0)\cos(\theta)+(y-y_0)\sin(\theta)]^2}{a^2} + \frac{[(x-x_0)\sin(\theta)-(y-y_0)\cos(\theta)]^2}{b^2} = 1, \tag{A.3a}$$

$$\begin{bmatrix} x_2 \\ y_2 \end{bmatrix} = \begin{bmatrix} 1 & 0 \\ 0 & \frac{1}{\lambda} \end{bmatrix} \begin{bmatrix} \cos(\theta) & -\sin(\theta) \\ \sin(\theta) & \cos(\theta) \end{bmatrix} \begin{bmatrix} x - x_0 \\ y - y_0 \end{bmatrix}, \tag{A.3b}$$

$$\lambda^2 = 1 - \varepsilon^2, \tag{A.3c}$$

$$\text{radius}_p = a, \tag{A.3d}$$

with a, b being the semi-axes in x and y of the ellipse centered in (x_0, y_0) and rotated θ degrees with excentricity ε. This way, each position $p = (x_p, y_p)$ has a corresponding $radius_p$ and a sun-blocking characteristics. The resulting sun-blocking characteristics of the cloud is depicted in Figure 2b.

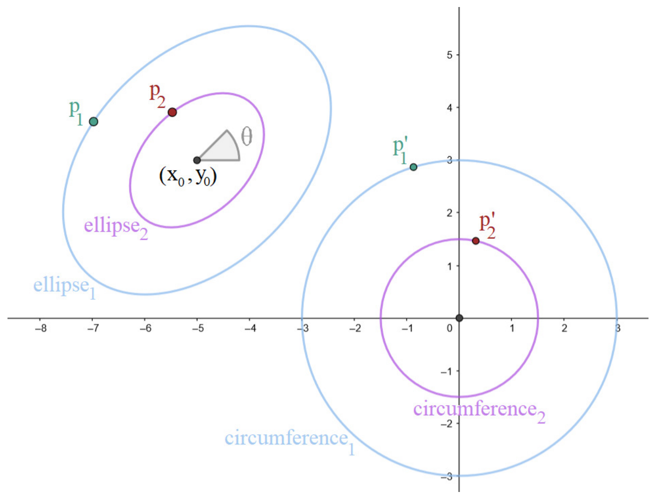

Figure A.22: Transformation from ellipse to circumference.

References

Academy, N., 2008. National academy of engineering. grand challenges for engineering. URL: `www.engineeringchallenges.org`.

ACS/Cobra Group, 2010. Extresol-1 (ex-1). `https://solarpaces.nrel.gov/extresol-1`. Accessed: 2021-03-10.

Aguilar-Lopez, J., Garcia, R., Camacho, E., 2021. Shape detection algorithm applicable to solar estimation. REVISTA IBEROAMERICANA DE AUTOMATICA E INFORMATICA INDUSTRIAL 18, 277–287.

Andrade, G.A., Pagano, D.J., Álvarez, J.D., Berenguel, M., 2013. A practical NMPC with robustness of stability applied to distributed solar power plants. Solar Energy 92, 106–122.

Besharat, F., Dehghan, A.A., Faghih, A.R., 2013. Empirical models for estimating global solar radiation: A review and case study. Renewable and Sustainable Energy Reviews 21, 798–821.

Blanco, M.J., Santigosa, L.R., 2017. Advances in Concentrating Solar Thermal Research and Technology. 1 ed., Woodhead Publishing. doi:`https://doi.org/10.1016/C2014-0-04054-3`.

Camacho, E.F., Berenguel, M., Rubio, F.R., Martínez, D., 2012. Control of Solar Energy Systems. Springer Science & Business Media.

Camacho, E.F., Gallego, A., 2013. Optimal operation in solar trough plants: A case study. Solar Energy 95, 106–117.

Camacho, E.F., Sánchez, A.J., Gallego, A.J., 2019. Solar Energy Systems: Progress and future directions. Nova Publishers. chapter Model Predictive Control of Large Scale Solar Trough Plants. pp. 1–59.

Dersch, J., Schroedter-Homscheidt, M., Gairaa, K., Hanrieder, N., Landelius, T., Lindskog, M., Mueller, S.C., Santigosa, L.R., Sirch, T., Wilbert, S., 2019. Impact of DNI nowcasting on annual revenues of CSP plants for a time of delivery based feed in tariff. Meteorologische Zeitschrift 28, 235–253.

DJI Technology Inc., 2015. Phantom 3 Pro user manual. https://dl.djicdn.com/downloads/phantom_3/en/Phantom_3_Professional_User_Manual__V1.6.pdf. Accessed: 2021-01-18.

Dorling, K., Heinrichs, J., Messier, G.G., Magierowski, S., 2016. Vehicle routing problems for drone delivery. IEEE Transactions on Systems, Man, and Cybernetics: Systems 47, 70–85.

European Commission, 2014. A policy framework for climate and energy in the period from 2020 up to 2030. Technical Report. European Commission. URL: https://eur-lex.europa.eu/legal-content/EN/TXT/PDF/?uri=CELEX:52014SC0015&from=EN.

European Commission, 2015. Energy Union Package: a framework strategy for a resilient Energy Union with a forward-looking climate change policy. Technical Report. European Commission. URL: https://ec.europa.eu/energy/sites/default/files/publication/FOR%20WEB%20energyunion_with%20_annex_en.pdf.

European Commission, 2018. Ocontsolar project – optimal control of thermal solar energy systems. URL: https://www.europeandissemination.eu/ocontsolar-project/2563.

Grimaccia, F., Aghaei, M., Mussetta, M., Leva, S., Quater, P.B., 2015. Planning for PV plant performance monitoring by means of unmanned aerial systems (UAS). International Journal of Energy and Environmental Engineering 6, 47–54.

Gu, J., Su, T., Wang, Q., Du, X., Guizani, M., 2018. Multiple moving targets surveillance based on a cooperative network for multi-UAV. IEEE Communications Magazine 56, 82–89.

Henk, M., 2012. Löwner-John ellipsoids. Documenta Math , 95–106.

Herceg, M., Kvasnica, M., Jones, C., Morari, M., 2013. Multi-Parametric Toolbox 3.0, in: Proc. of the European Control Conference, Zürich, Switzerland. pp. 502–510. http://control.ee.ethz.ch/~mpt.

Islam, M.T., Huda, N., Abdullah, A.B., Saidur, R., 2018. A comprehensive review of state of the art concentrating solar power (CSP) technologies: Current status and research trends. Renewable and Sustainable Energy Reviews 91, 987–1018.

Kannan, N., Vakeesan, D., 2016. Solar energy for future world: A review. Renewable and Sustainable Energy Reviews 62, 1092–1105.

Khachiyan, L.G., 1996. Rounding of polytopes in the real number model of computation. Mathematics of Operations Research 21, 307–320.

Kuhn, P., Wilbert, S., Prahl, C., Schüler, D., Haase, T., Hirsch, T., Wittmann, M., Ramirez, L., Zarzalejo, L., Meyer, A., et al., 2017. Shadow camera system for the generation of solar irradiance maps. Solar Energy 157, 157–170.

Li, A., 2020. Approximate Lowner ellipsoid. https://www.mathworks.com/matlabcentral/fileexchange/21930-approximate-lowner-ellipsoid.

Liu, Z., Sengupta, R., Kurzhanskiy, A., 2017. A power consumption model for multi-rotor small unmanned aircraft systems, in: 2017 International Conference on Unmanned Aircraft Systems (ICUAS), IEEE. pp. 310–315.

Mademlis, I., Mygdalis, V., Nikolaidis, N., Montagnuolo, M., Negro, F., Messina, A., Pitas, I., 2019. High-level multiple-UAV cinematography tools for covering outdoor events. IEEE Transactions on Broadcasting 65, 627–635.

Matuszko, D., 2012. Influence of the extent and genera of cloud cover on solar radiation intensity. International Journal of Climatology 32, 2403–2414.

Minis, N., Rosenbluth, E., Hayut, R., Am-Shallem, M., 2019. Spatial DNI measurement for accurate solar flux control in Megalim 121MWe solar receiver power plant, in: AIP Conference Proceedings, AIP Publishing LLC. p. 030037.

Montes, M., Abánades, A., Martínez-Val, J., Valdés, M., 2009. Solar multiple optimization for a solar-only thermal power plant, using oil as heat transfer fluid in the parabolic trough collectors. Solar Energy 83, 2165 – 2176.

Quater, P.B., Grimaccia, F., Leva, S., Mussetta, M., Aghaei, M., 2014. Light unmanned aerial vehicles (UAVs) for cooperative inspection of PV plants. IEEE Journal of Photovoltaics 4, 1107–1113.

Quesada-Ruiz, S., Chu, Y., Tovar-Pescador, J., Pedro, H., Coimbra, C., 2014. Cloud-tracking methodology for intra-hour DNI forecasting. Solar Energy 102, 267–275.

Rokhmana, C.A., 2015. The potential of UAV-based remote sensing for supporting precision agriculture in Indonesia. Procedia Environmental Sciences 24, 245–253.

Sánchez, A.J., Gallego, A.J., Escaño, J.M., Camacho, E.F., 2018a. Event-based MPC for defocusing and power production of a parabolic trough plant under power limitation. Solar Energy 174, 570 – 581.

Sánchez, A.J., Gallego, A.J., Escaño, J.M., Camacho, E.F., 2018b. Temperature homogenization of a solar trough field for performance improvement. Solar Energy 165, 1–9.

Sánchez, A.J., Gallego, A.J., Escaño, J.M., Camacho, E.F., 2019. Thermal balance of large scale parabolic trough plants: A case study. Solar Energy 190, 69 – 81.

Silvagni, M., Tonoli, A., Zenerino, E., Chiaberge, M., 2017. Multipurpose UAV for search and rescue operations in mountain avalanche events. Geomatics, Natural Hazards and Risk 8, 18–33.

Solar Mems Technologies, 2019. Sun Sensor NANO-ISSX/c technical specifications. $http://www.solar-mems.com/smt_pdf/NANO_Technical_Specifications.pdf$. Accessed: 2020-08-18.

Solar Millennium, A., 2018. The construction of the andasol power plants. Solar Millennium .

Zhang, Y., 2020. A maximum volume ellipsoid finder. https://www.mathworks.com/matlabcentral/fileexchange/59395-a-maximum-volume-ellipsoid-finder.

Zhang, Y., Gao, L., 2003. On numerical solution of the maximum volume ellipsoid problem. SIAM Journal on Optimization 14, 53–76.